



日本原子力研究開発機構機関リポジトリ  
Japan Atomic Energy Agency Institutional Repository

Title	Cs-Te corrosion depth dependence on distribution of chromium carbide precipitation in high chromium steel
Author(s)	Sasaki Koei, Fujimura Ryota, Tanigaki Takanori, Matsubara Masanori, Fukumoto Kenichi, Uno Masayoshi
Citation	Journal of Nuclear Science and Technology, 54(2), p.139-146
Text Version	Author's Post-print
URL	<a href="https://jopss.jaea.go.jp/search/servlet/search?5056741">https://jopss.jaea.go.jp/search/servlet/search?5056741</a>
DOI	<a href="https://doi.org/10.1080/00223131.2016.1214628">https://doi.org/10.1080/00223131.2016.1214628</a>
Right	This is an Accepted Manuscript of an article published by Taylor & Francis in Journal of Nuclear Science and Technology on February 2017, available online: <a href="http://www.tandfonline.com/10.1080/00223131.2016.1214628">http://www.tandfonline.com/10.1080/00223131.2016.1214628</a> .

**Cs-Te corrosion depth dependence on distribution of chromium carbide precipitation in high chromium steel**

Koei Sasaki<sup>a,b\*</sup>, Ryota Fujimura<sup>b</sup>, Takanori Tanigaki<sup>a</sup>, Masanori Matsubara<sup>b</sup>,  
Ken-ichi Fukumoto<sup>b</sup> and Masayoshi Uno<sup>b</sup>

<sup>a</sup> *Japan Atomic Energy Agency, 2-1, Shiraki, Tsuruga-shi, Fukui 919-1279, Japan;*

<sup>b</sup> *Research Institute of Nuclear Engineering, University of Fukui, 1-2-4 Kanawa-cho,  
Tsuruga, Fukui 914-0055, Japan*

In an attempt to investigate Cs-Te corrosion depth dependence on distribution of chromium carbide precipitation in high chromium steel, Cs-Te corrosion out-pile tests of two 9Cr steels with different distributions of chromium carbide were carried out at 975K for 100h and their corrosion depths were compared. The corrosion is obviously more advanced in a specimen which has grain boundary carbide than in the one that doesn't. A considerable reason of the result is that the carbide distributed at grain boundaries promoted the corrosion reaction and the corrosion extended along the grain boundary. This is the first case in which the Cs-Te corrosion depth dependence on distribution of chromium carbide precipitation in Fe-Cr steel is clarified experimentally.

***Keywords; FBR; fuel cladding; FCCI; corrosion; cesium telluride; high burnup fuel***

---

\*Corresponding author. Email: sasaki.koei@jaea.go.jp

## 1. Introduction

Development of the cladding material which has high resistance to irradiation swelling and fuel-cladding chemical interaction (FCCI) is required for burn-ups enhancement in Fast Breeder Reactor (FBR) fuel pin. [1, 2].

Fe-Cr steel is developed as candidate material for FBR fuel cladding [3, 4]. And the chemical composition and microstructure has been optimized based on irradiation resistance and high-temperature mechanical property [1]. FCCI resistance of FBR fuel cladding material is also necessary for further development of burn-ups. Post irradiation examination results in JOYO showed that Fe-Cr steel was obviously attacked and thinned by FCCI [5, 6]. Moreover, clad wastage correlations predicted several hundred micro meters depth of FCCI attack depending on calculation condition [7]. Many studies about FCCI in austenitic stainless steel claddings such as in-pile tests, out-pile tests and their related fundamental researches were carried out mostly in 1970s. Fe-Cr ferritic steel took the place of austenitic stainless steel as a candidate material for FBR fuel cladding after it was found that ferric steel has excellent swelling resistance under high dose neutron irradiation [8]. FCCI behavior dependence on material factors such as chemical composition and microstructure of the cladding have not been investigated yet although they are necessary to improve FCCI resistance of the material.

Main causative agents of FCCI in oxide fuel pin were estimated to be Cs and Te based on thermodynamic consideration by Adamson [9].

In addition, a past experimental report suggested that decomposition of chromium carbide at grain boundary by tellurium in cesium telluride can advance the Cs-Te corrosion in high chromium steel [10]. In an attempt to investigate Cs-Te corrosion depth dependence on distribution of chromium carbide precipitation in high chromium steel, Cs-Te corrosion out-pile tests of two 9Cr steels with different distributions of chromium carbide were carried out.

This report is the first case to investigate the relation between Cs-Te corrosion depth and distribution of chromium carbide precipitation in Fe-Cr steel.

## 2. Experimental

### 2.1. Material

#### 2.1.1. Metallographic structure

A Fe-9Cr-0.1C ternary ingot was alloyed by arc melting and cold worked up to rolling ratio of 50% at room temperature (RT). The ingot was cut into halves. A half, hereinafter referred to as 9Cr-0.1C(A), was isothermal-treated at 1073K for 1h and cooled to RT in 10h. The heat treatment makes the supersaturated C and Cr in the material to precipitate in grain. Another half, hereinafter referred to as 9Cr-0.1C(B), was heated up to 1273K in 20h and cooled to RT in 10h. The heat treatment assists microsegregation of carbon along grain boundary in order to precipitate chromium carbide at the specimen's grain boundary.

Figure 1 shows scanning electron microscope (SEM) images of electrolytic-polished surfaces of the specimens. The electrolytic polishing condition is HClO<sub>4</sub> solution

(HClO<sub>4</sub>:CH<sub>3</sub>COOH solvent = 1:9) with 36 V at room temperature. Brightened spots in the images are precipitations. 9Cr-0.1C(A) has precipitation mainly distributed in the alloy matrix and 9Cr-0.1C(B) has precipitation mainly distributed at the grain boundary network. Both specimens have nearly the same average grain sizes approximately 30 $\mu$ m which are measured by line segment method of 1.6mm<sup>2</sup> area of each specimen.

< Figure 1 (a)> A SEM image of electrolytic-polished surface of 9Cr-0.1C(A).

< Figure 1 (b)> A SEM image of electrolytic-polished surface of 9Cr-0.1C(B).

### 2.1.2. Precipitates in the material

Figure 2 shows (a) a transmission electron microscope (TEM) image, (b) an EDS spectrum and (c) an electron diffraction pattern of precipitates in 9Cr-0.1C(A). Very fine precipitates which have a diameter of 100 ~ 200nm were observed as shown in Figure 2 (a). An EDS spectrum of a precipitate  $\alpha$  in Figure 2 (a) was obtained by TEM as shown in Figure 2 (b) and it's suggested that the precipitate  $\alpha$  consists of mainly chromium and carbon. The Cu detection in the spectrum is caused by energy refraction from TEM mesh made of copper. Figure 2 (c) shows an electron diffraction pattern of the precipitate  $\alpha$ . The diffraction pattern spot arrangement matched Cr<sub>23</sub>C<sub>6</sub> [11]. The Fe detection in the spectrum must be from base metal near the precipitate  $\alpha$ .

Figure 3 shows (a) a TEM image, (b) an EDS spectrum and (c) an electron diffraction pattern of precipitates in 9Cr-0.1C(B). Figure 3 (a) shows that the precipitates were distributed in the form of a continuous line. Precipitate  $\beta$  in Figure 3 (a) was analyzed and specified as chromium carbide Cr<sub>23</sub>C<sub>6</sub> [11] based on an EDS spectrum (Figure 3 (b)) and an electron diffraction pattern (Figure 3 (c)) in the same way as precipitate  $\alpha$  in Figure 2.

< Figure 2 (a) > A TEM image of precipitates in 9Cr-0.1C(A).

< Figure 2 (b)> An EDS spectrum of the precipitate  $\alpha$  in Figure 2 (a).

< Figure 2 (c)> An electron diffraction pattern of the precipitate  $\alpha$  in Figure 2 (a).

< Figure 3 (a)> A TEM image of precipitates in 9Cr-0.1C(B).

< Figure 3 (b)> An EDS spectrum of the precipitate  $\beta$  in Figure 3 (a).

< Figure 3 (c)> An electron diffraction pattern of the precipitate  $\beta$  in Figure 3 (a).

### 2.2. Cs-Te corrosion test

Cylindrical shaped specimens ( $\Phi = 3.7 \text{ mm} \times l = 20 \text{ mm}$ ) were cut out from the ingot after the heat treatment as written in the section 2.1.1. The surfaces were polished by sand papers (~ #15000) and diamond grains (~0.25  $\mu$ m). Figure 4 shows an illustration of the Cs-Te corrosion test apparatus. The entire process of assembling apparatus including synthesizing Cs-Te corrosive compound was carried out in an argon filled glove-bag. The

Cs-Te corrosive compound was synthesized by mixing liquid cesium (99.95%, Sigma-Aldrich) and tellurium powder (99.8%, Sigma-Aldrich) in the ratio of 1:1 in the glove-bag. Figure 5 shows an X-Ray Diffraction pattern of the Cs-Te corrosive compound and the compound was mainly  $\text{Cs}_2\text{Te}_3$  [12]. The Te-activity value of  $\text{Cs}_2\text{Te}_3$  is equivalent to the Te-activity in  $\text{MO}_x$  ( $M=\text{U}_{0.75}\text{Pu}_{0.25}$ ,  $x>2$ ) [13] which can simulate sufficient amount of severity of the corrosion environment in high burn-up FBR fuel pin. The specimens and  $\text{Cs}_2\text{Te}_3$  were put into an alumina crucible. The crucible and Mo/MoO<sub>2</sub> mixed powder (Mo:MoO<sub>2</sub> = 1:1, 1.5g) were put into a one end sealed quartz tube to simulate an oxygen potential of high burn-up FBR fuel pin inert gas (-416.5 kJ/mol at 923K) [14]. Next, the other open end of the quartz tube was sealed with an attached valve and the quartz tube was taken out from the glove-bag. The quartz tube was heated in an electric furnace up to 923 K for 100 hours as the corrosion test. The corrosion area on the cross-sections were observed by SEM with EDS and all corrosion depths in the cross-sections were measured by SEM.

< Figure 4 > An illustration of the Cs-Te corrosion test apparatus.

< Figure 5 > An X-Ray Diffraction pattern of the Cs-Te corrosive compound.

### 3. Result

#### 3.1. Nature of Corrosion

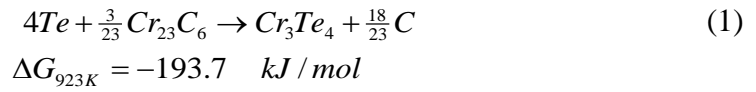
Figure 6 (a) shows SEM images and EDS mapping images of cross-section of the specimens after the corrosion test. Each interval of line shaped corrosion areas is several tens micro meters in Figure 6 whose value is close to the grain size shown in Figure 1. The corrosion area seems to be extended along the grain boundary in both specimens. Figure 6 (b) shows magnified SEM images and EDS line profiles of area A1 and B1 in Figure 6 (a). Stronger detection of Cr, Cs and Te from corroded areas and weaker detection of Cr in the vicinity of the corroded areas can be seen in both EDS mapping images (Figure 6 (a)) and EDS line profiles (Figure 6 (b)). The observation result corresponds to typical Cs-Te corrosion [10, 15]. Cs and Te detections on the 9Cr-0.1C(A) surface are from the Cs-Te corrosive compound adhered during the corrosion test. Fe layer and Cr-O layer near the specimen surface are caused by selective oxidation of chromium in the controlled test atmosphere (the oxygen potential is approximately -416.5 kJ/mol at 923K). The test condition can oxidize only chromium in the Fe-Cr alloy and make non-oxidized Fe to precipitate on the surface according to a past reference [16].

< Figure 6 (a) > SEM images and EDS mapping images of cross-section of the specimens after the corrosion test.

< Figure 6 (b) > Magnified SEM images and EDS line profiles of area A1 and B1 in Figure 6 (a).

#### 3.2. Cs-Te corrosion product

A part of corroded area as seen in Figure 6 was extracted from each specimen and fabricated to TEM samples by Focus Ion Beam method. Figure 7 shows (a) a TEM image and EDS mapping images of a part of corroded area in 9Cr-0.1C(A), (b) an electron diffraction pattern of the corrosion product **A** in the TEM image. Figure 8 shows (a) a TEM image and EDS mapping images of a part of corroded area in 9Cr-0.1C(B), (b) an electron diffraction pattern of the corrosion product **B** in the TEM image. Striated Cr-Te-Cs area next to Fe-Cr base material can be seen in both Figure 7 (a) and Figure 8 (a). Diffraction pattern spot arrangement matched the one of Cr-Te compound, Cr<sub>3</sub>Te<sub>4</sub> [17] of all reported Cs-Cr-Te compounds (CsCr<sub>5</sub>Te<sub>8</sub>[18], Cr<sub>0.67</sub>Te[19], Cr<sub>0.83</sub>Te[20], Cr<sub>2</sub>Te<sub>3</sub>[20], Cr<sub>3</sub>Te<sub>4</sub>[17], Cr<sub>5</sub>Te<sub>8</sub>-monoclic[20], Cr<sub>5</sub>Te<sub>8</sub>-trigonal[21], Cr<sub>7</sub>Te<sub>8</sub>[22], CrTe[23], CrTe<sub>3</sub>[24]). Energy value of a Te peak (Lβ<sub>2</sub>: 4.301 keV) is near a Cs peak (Lα<sub>1</sub>: 4.286 keV) which should be noted in this regard. As a result, the corrosion products both **A** and **B** can be specified as Cr<sub>3</sub>Te<sub>4</sub>, and the result corresponds to assumable corrosion reactions shown below according to a past reference [10].



< Figure 7 (a)> A TEM image and EDS mapping images of a part of corroded area in 9Cr-0.1C(A).

< Figure 7 (b)> An electron diffraction pattern of the corrosion product **A** in Figure 7 (a).

< Figure 8 (a)> A TEM image and EDS mapping images of a part of corroded area in 9Cr-0.1C(B).

< Figure 8 (b)> An electron diffraction pattern of the corrosion product **B** in Figure 8 (a).

### 3.3. Corrosion depth

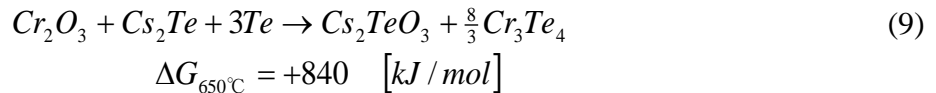
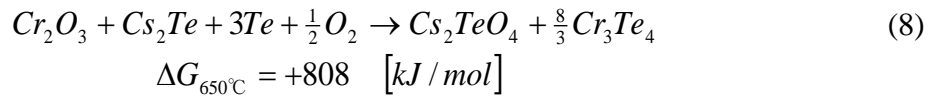
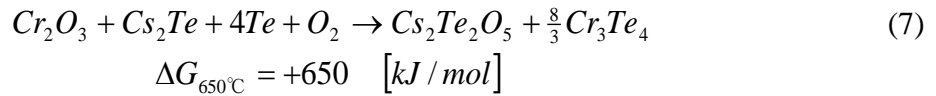
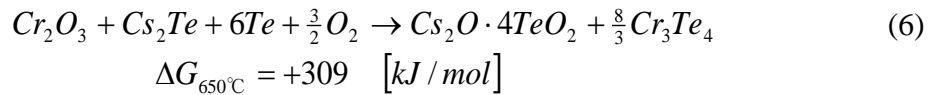
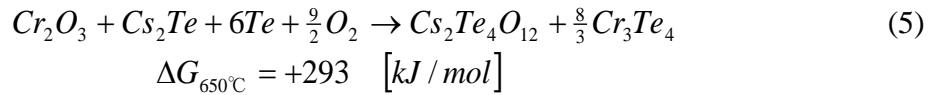
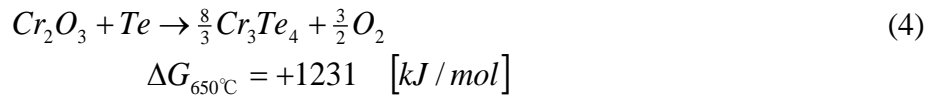
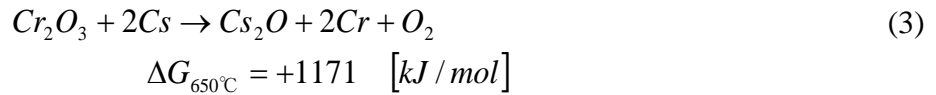
Figure 9 shows histograms of corrosion extension depth in 9Cr-0.1C(A) and (B).

The distance between the specimen surface and the deepest edge of intergranular corrosion was defined as the corrosion depth in this report. The frequency axis of the histograms represents the number of Cs-Te corrosion edges on the entire cross-section of the specimen. The corrosion is obviously more advanced in 9Cr-0.1C(B) than in 9Cr-0.1C(A). A considerable reason of the result is that the ranged chromium carbide at grain boundaries as shown in Fig.1(b) promoted the Eq.(1) and the corrosion in 9Cr-0.1C(B) extended more along the grain boundary than 9Cr-0.1C(A). This experimental result suggests that to avoid forming chromium carbide at grain boundaries in cladding material can suppress the Cs-Te corrosion extension which is one of the main factors of FCCI in FBR.

< Figure 9 > Histogram of corrosion depth in 9Cr-0.1C(A) and (B).

#### 4. Discussion

Figure 10 (a) shows illustrations of cross-section of the specimens before the corrosion test. As written in the section 2.1.1, 9Cr-0.1C(A) has precipitation mainly distributed in the alloy matrix and 9Cr-0.1C(B) has precipitation mainly distributed at grain boundary network. Since the corrosion was observed in both specimens, normally Fe-Cr alloy was covered by passive oxidation film  $Cr_2O_3$  which cannot react with cesium, tellurium or cesium tellurides as shown below (Eq.(3)~(9)). The  $Cr_2O_3$  film might be damaged by sensitization during the corrosion test at 953K at the precipitations. On the 9Cr-0.1C(B) surface, practically grain boundary could be sensitized. On the 9Cr-0.1C(A) surface, some part of the grain boundary which has the precipitation could also be sensitized. The corrosion can start from the sensitized part of the specimen surface along the precipitation distribution.



< Figure 10 (a) > Illustrations of cross-section of the specimens before the corrosion test.

Figure 10 (b) shows illustrations of cross-section of the specimens after the corrosion test. A Fe/Cr-O layer on the surface and intergranular corrosion was observed in both specimens. The

layer was formed by selective oxidation of Cr in the controlled test atmosphere as mentioned in the section 3.1. The formation reaction is not linked to the Cs-Te corrosion reaction such as Eq.(1) or (2).

The precipitation distribution in 9Cr-0.1C(B) has stronger dependence on grain boundary texture than in 9Cr-0.1C(A). It can advance the Cs-Te corrosion reaction Eq.(1) in 9Cr-0.1C(B) more than in 9Cr-0.1C(A).

< Figure 10 (b) > Illustrations of cross-section of the specimens after the corrosion test.

## 5. Conclusion

Cs-Te corrosion out-pile tests of two 9Cr steels with different distributions of chromium carbide were carried out at 975K for 100h and their corrosion depths were compared.

Corrosion products in both specimens after the test were specified as  $Cr_3Te_4$ . Therefore  $4Te + \frac{3}{23}Cr_{23}C_6 \rightarrow Cr_3Te_4 + \frac{18}{23}C$  and  $4Te + 3Cr \rightarrow Cr_3Te_4$  can be presumable corrosion reactions the same as previously reported reactions [10].

The corrosion is obviously more advanced in a specimen which has grain boundary carbide than in the one that doesn't. A considerable reason of the result is that the ranged carbide at grain boundaries promoted the corrosion reaction  $4Te + \frac{3}{23}Cr_{23}C_6 \rightarrow Cr_3Te_4 + \frac{18}{23}C$  and the corrosion extended along the grain boundary. This experiment result made it clear that chromium carbides at grain boundary can advance the Cs-Te corrosion in Fe-Cr steel.

## Acknowledgements

This work is partly supported by the "Joint Usage/Research Program on Zero-Emission Energy Research, Institute of Advanced Energy, Kyoto University (ZE25A5, ZE26A14 and ZE27A24) and "Core R&D program for commercialization of the fast breeder reactor by utilizing Monju" entrusted to University of Fukui by the Ministry of Education, Culture, Sports, Science and Technology of Japan (MEXT).

## Reference

- [1] Cheon JS, Lee CB, Lee BO, Raison JP, Mizuno T, Delage F, Carmack J, Sodium fast reactor evaluation: Core materials. J. Nucl. Mater. 2009; 392: 324-330.
- [2] Maeda K, Comprehensive Nuclear Materials vol. 3: Advanced Fuels/Fuel Cladding/Nuclear Fuel Performance Modeling and Simulation. Japan: Elsevier Science Limited; 2012. Ceramic Fuel-Cladding Interaction; 443-483.
- [3] Klueh RL, Nelson AT, Ferritic/martensitic steels for next-generation reactors. J. Nucl. Mater. 2007; 371: 37-52.
- [4] Ukai S, Nishida T, Okuda T, Yoshitake T, R&D of oxide dispersion strengthened ferritic martensitic steels for FBR. J. Nucl. Mater. 1998; 258-263: 1745-1749.
- [5] Maeda K, Tanaka K, Agasa T, Furuya H, Distributions of volatile fission products in

or near the fuel-cladding gap of the FBR MOX fuel pins irradiated to high burn-up. *J. Nucl. Mater.* 2005; 344: 274-280.

[6] Tanaka K, Maeda K, FCCI behavior of high-strength ferritic/martensitic steel (PNC-FMS) cladding fuel pins Results of interim post irradiation examinations of FMS-1 irradiation test. Japan: Nuclear Cycle Development Institute; 2009.

[7] Viswanathan R, Fuel clad chemical interactions in fast reactor MOX fuels. *J. Nucl. Mater.* 2014; 444: 101-111.

[8] Gells DS, Swelling in several commercial alloys irradiated to very high neutron fluence. *J. Nucl. Mater.* 1984; 122 & 123: 207-213.

[9] Adamson MG, Aitken EA, On the Cs,Te fission product-induced attack and embrittlement of stainless steel cladding in oxide fuel pins. *J. Nucl. Mater.* 1985; 132: 160-166.

[10] Sasaki K, Tanigaki T, Fujimura R, Fukumoto K, Uno M, The corrosion product of Cs-Te corrosive compound with 11Cr-Ferritic/Martensitic Steel and 9Cr-Oxide Dispersion Strengthened steel. *J. Nucl. Mater.* 2015; 460: 107-113.

[11] Berkane R, Gachon JC, Charles J, Hertz J, A thermodynamic study of the chromium-carbon system. *Calphad.* 1987; 11: 375-382.

[12] Chuntunov KA, Orlov AN, Yatsenko SP, Grin YN, Miroshnikova LD, Synthesis of Chalcogenides Having the Composition  $A_2B_3$  and Crystal Structure of  $Rb_2Te_3$  and  $Cs_2Te_3$ . *Izv. Akad. Nauk SSSR, Neorg. Mater.* 1982; 18 7: 1113-1116.

[13] Adamson MG, Aitken EA, Lindemer TB, Chemical thermodynamics of Cs and Te fission product interactions in irradiated LMFBR mixed-oxide fuel pins. *J. Nucl. Mater.* 1985; 130: 375-392.

[14] Park K, Yang MS, The stoichiometry and the oxygen potential change of urania fuels during irradiation. *J. Nucl. Mater.* 1997; 247: 116-120.

[15] Pulham RJ and Richards MW, Chemical reactions between caesium, tellurium and oxygen with fast breeder reactor cladding alloys Part 3 – The effect of oxygen potential on the corrosion by caesium-tellurium mixtures. *J. Nucl. Mater.* 1990; 172: 206-219.

[16] Sato I, Takaki M, Arima T, Furuya H, Idemitsu K, Inagaki Y, Momoda M, Namekawa T, Oxidation behavior of modified SUS316 (PNC316) stainless steel under low oxygen partial pressure, *J. Nucl. Mater.* 2002; 304: 21–28.

[17] Ohta S, Kaneko T, Yoshida H, Anisotropic thermal expansion and effect of pressure on magnetic transition temperatures in chromium chalcogenides  $Cr_3X_4$  with  $X = Se$  and  $Te$ . *J. Magn. Mater.* 1996; 163: 117-124.

[18] Ohtani T, Sano Y, Kodama K, Onoue S, Nishihara H, SYNTHESIS OF NEW TERNARY TUNNEL CHALCOGENIDES BY ION EXCHANGE REACTIONS AND DEINTERCALATION OF THE TERNARY CHROMIUM STEELS, *Mat. Res. Bull.* 1993; 28: 501-508.

[19] M. Yuzuri, Y. Adachi, T. Kaneko, H. Yoshida, S. Abe, Pressure effect on the Neel temperature of  $Cr_2Te_{3-x}Se_x$ , *J. Magn. Mater.* 1995; 140-144: 151-152.

[20] Ipser H, Komarek K, Klepp K, TRANSITION METAL-CHALCOGEN SYSTEMS VIII: THE Cr-Te PHASE DIAGRAM, *J. Less Common Met.* 1983; 92: 265-282.

- [21] Hatakeyama K, Kaneko T, Yoshida H, Ohta S, Anzai S, Pressure effect on the Curie temperature of  $\text{Cr}_{1-\delta}\text{Te}$  compounds, *J. Magn. Magn. Mater.* 1990; 90-91: 175-176.
- [22] Yuzuri M, Nakagawa T, Sugimoto M, Magnetic properties of annealed and quenched  $\text{Cr}_7\text{Se}_{8-x}\text{Te}_x$  system, *J. Magn. Magn. Mater.* 1992; 104-107: 885-886.
- [23] Ohta S, Kanomata T, Kaneko T, Yoshida H, Pressure effect on Curie temperature and thermal expansion of  $\text{CrTe}$ , *J. Phys. Condens. Matter.* 1983; 5: 2759-2768.
- [24] Klepp K, Ipsen H, On the Phase  $\text{CrTe}_3$ , *Mh. Chem.* 1979; 110: 499-501.

**Figure captions (one column)**

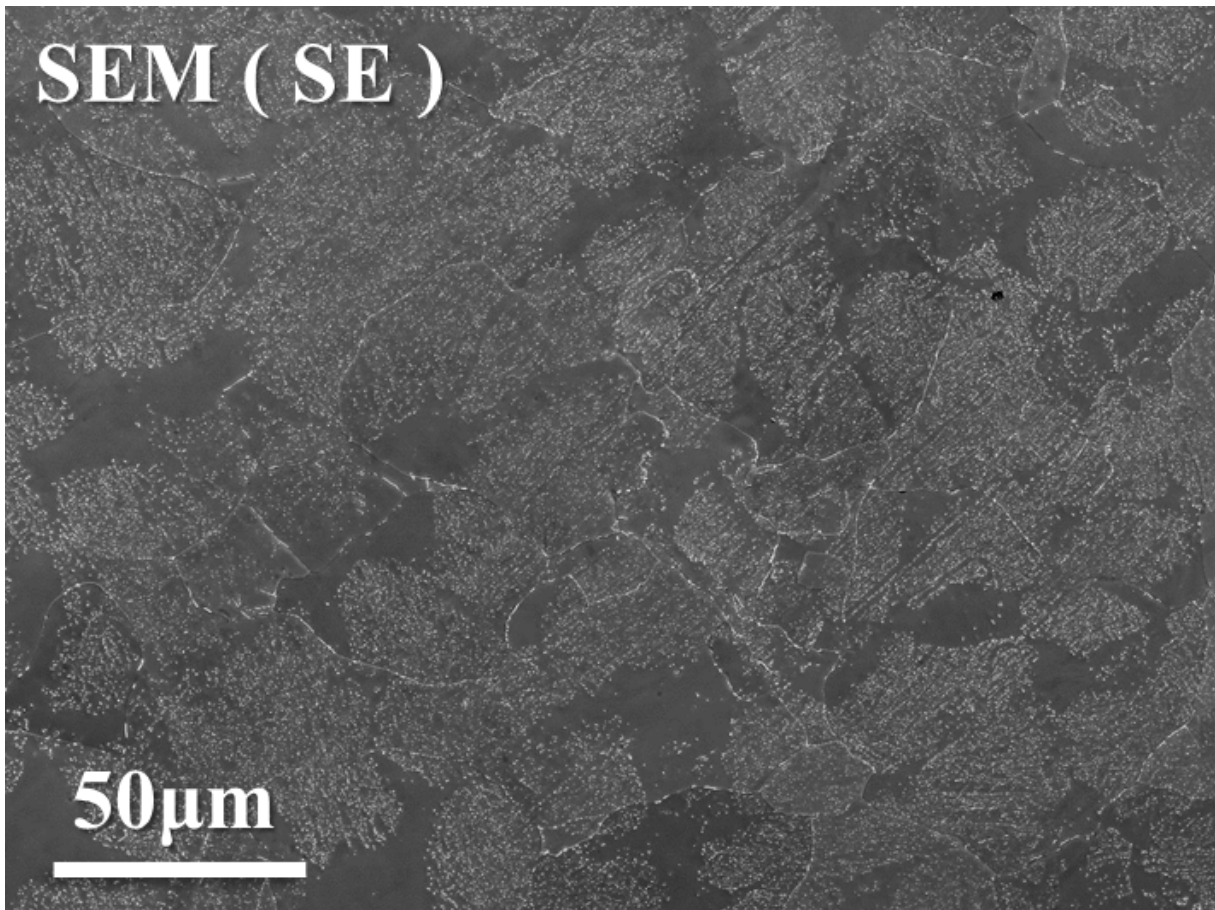


Figure 1 (a). A SEM image of electrolytic-polished surface of 9Cr-0.1C(A).

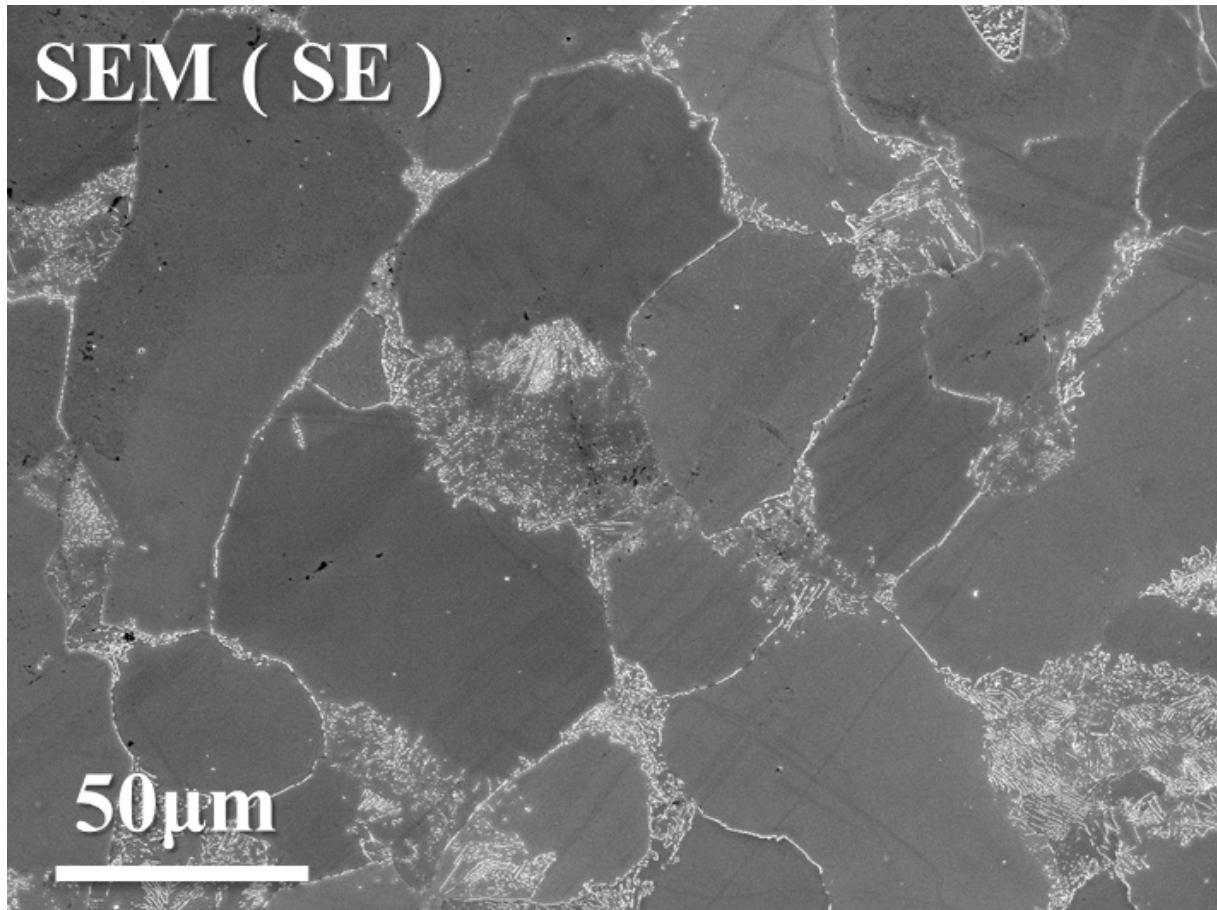


Figure 1 (b). A SEM image of electrolytic-polished surface of 9Cr-0.1C(B).

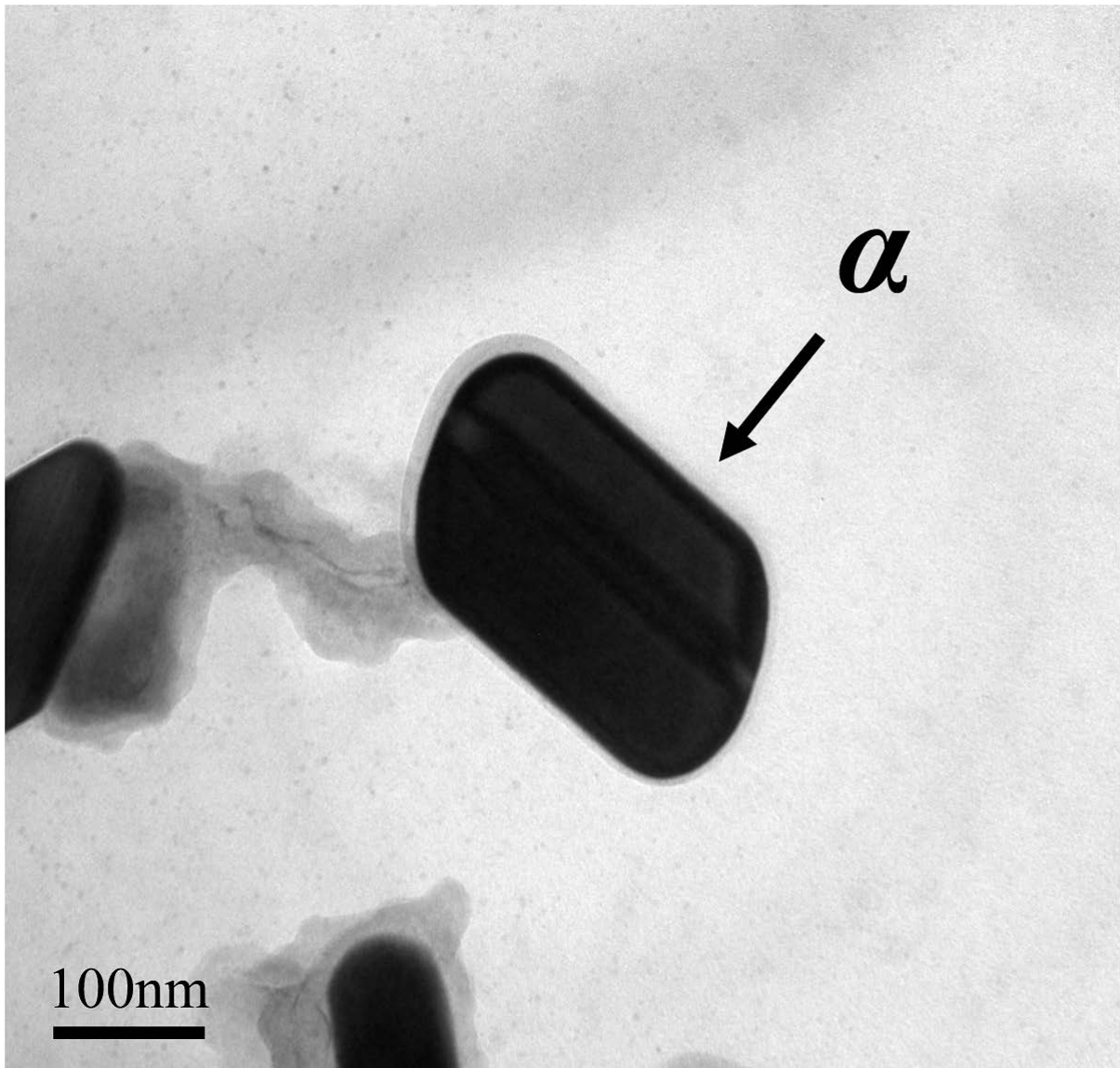


Figure 2 (a). A TEM image of precipitates in 9Cr-0.1C(A).

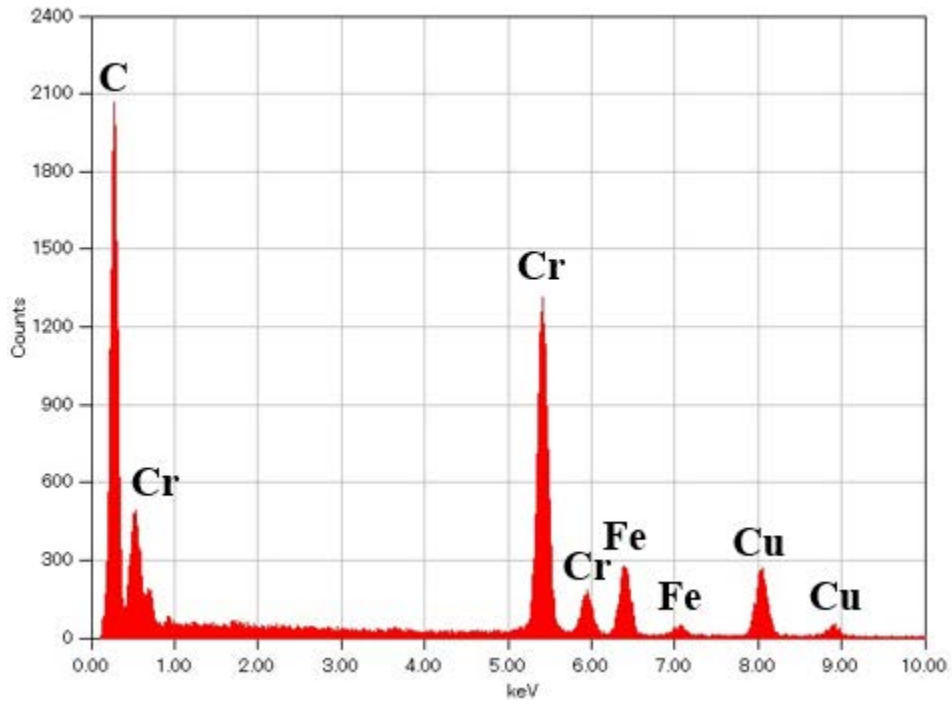


Figure 2 (b). An EDS spectrum of the precipitate  $\alpha$  in Figure 2 (a).

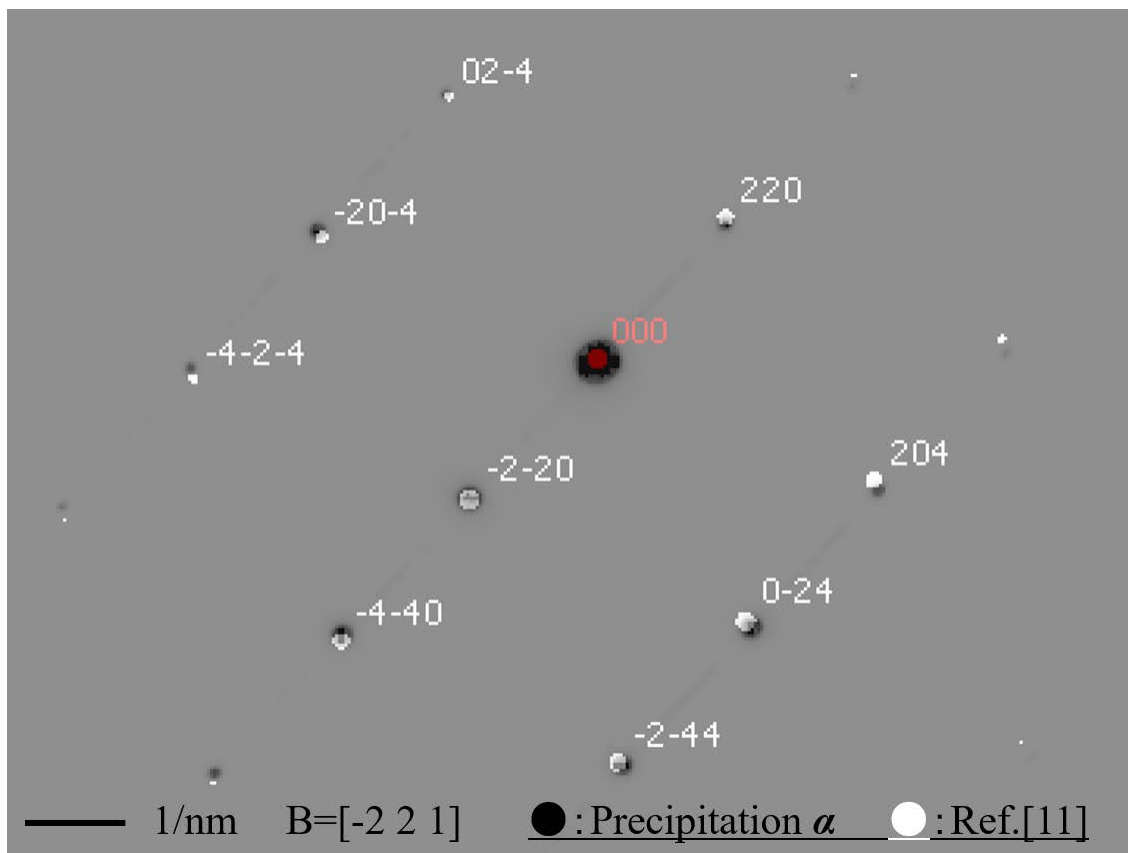


Figure 2 (c). An electron diffraction pattern of the precipitate  $\alpha$  in Figure 2 (a).

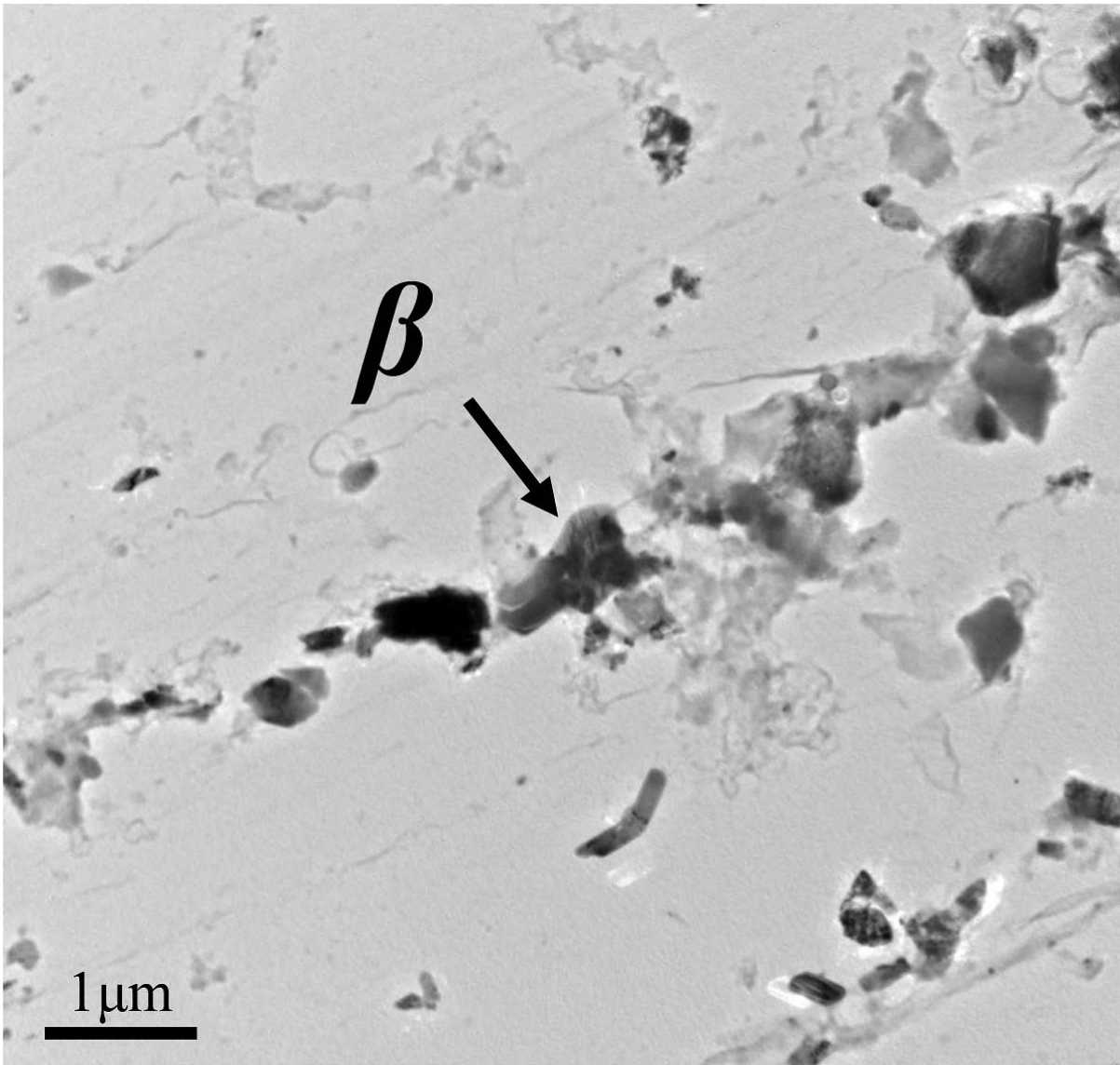


Figure 3 (a). A TEM image of precipitates in 9Cr-0.1C(B).

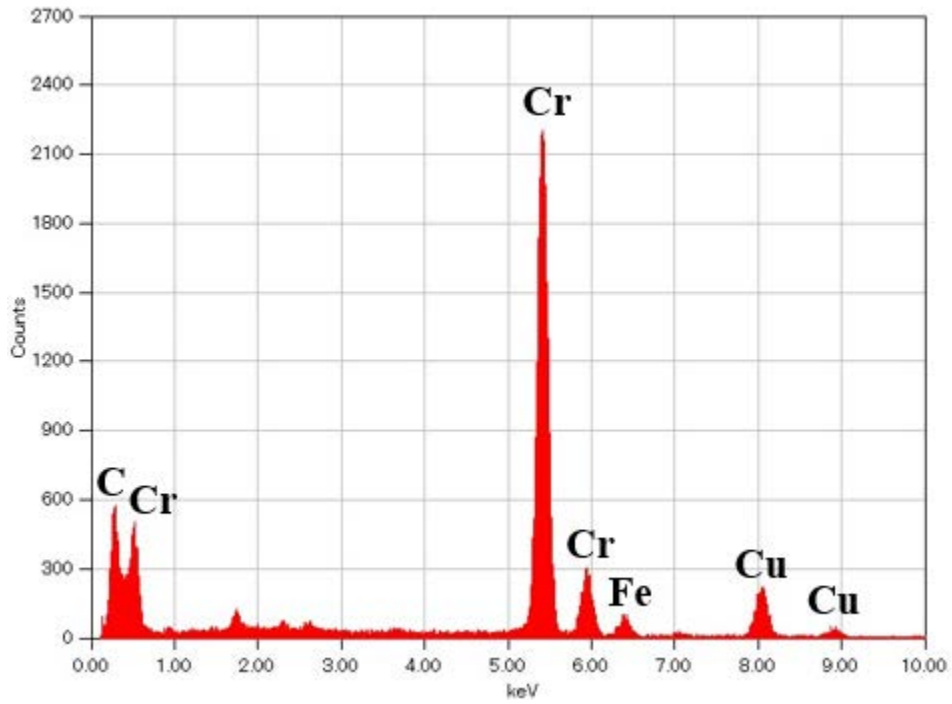


Figure 3 (b). An EDS spectrum of the precipitate  $\beta$  in Figure 3 (a).

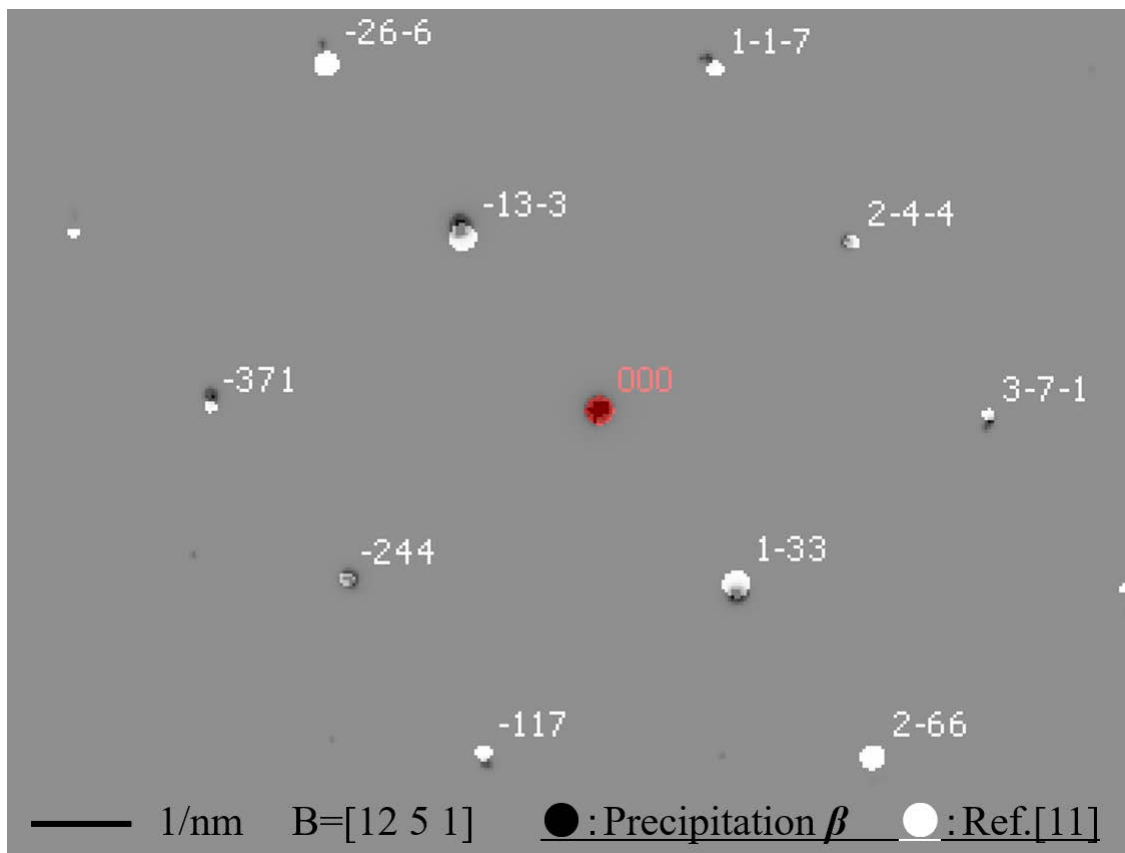


Figure 3 (c). An electron diffraction pattern of the precipitate  $\beta$  in Figure 3 (a).

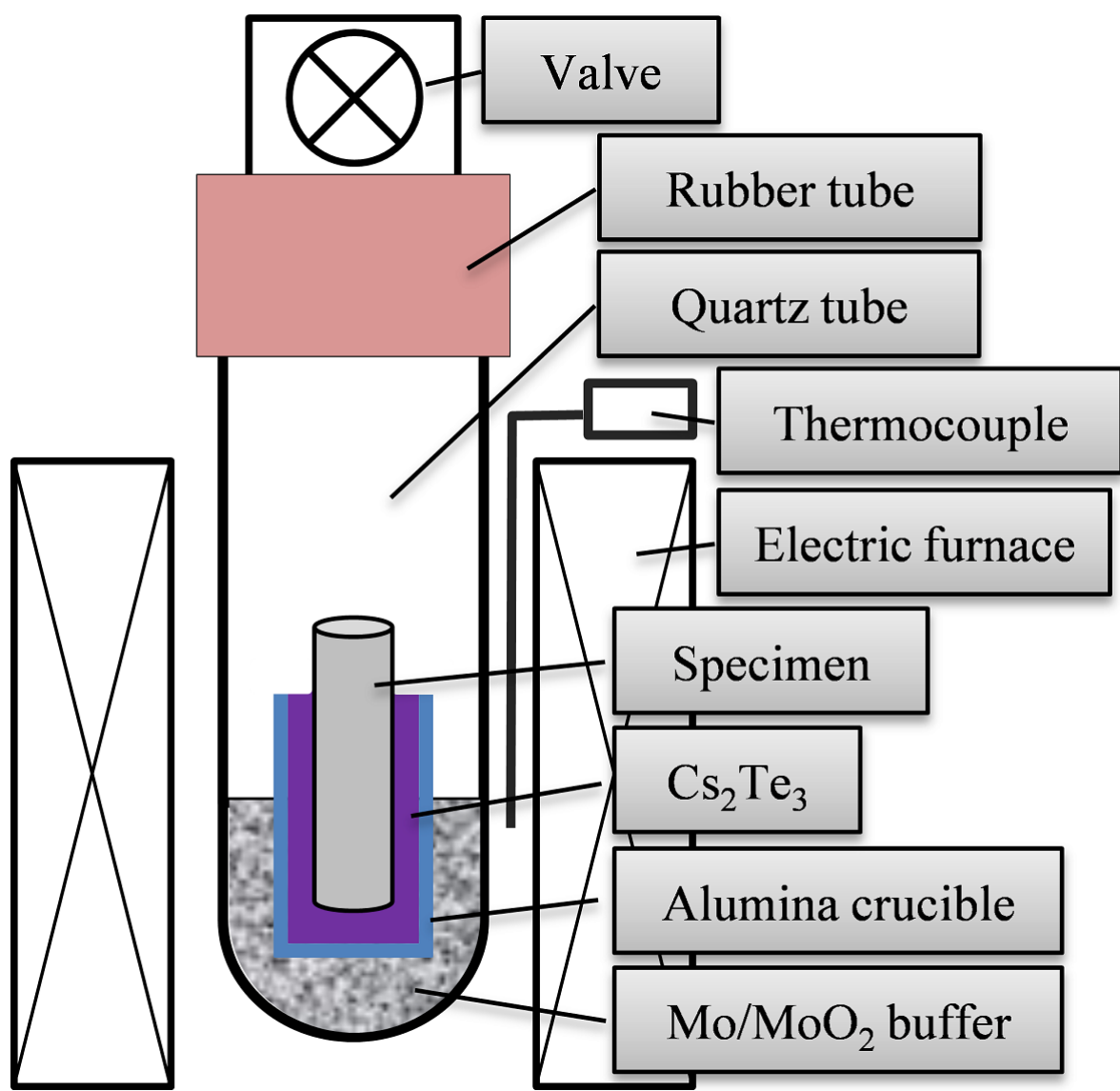


Figure 4. An illustration of the Cs-Te corrosion test apparatus.

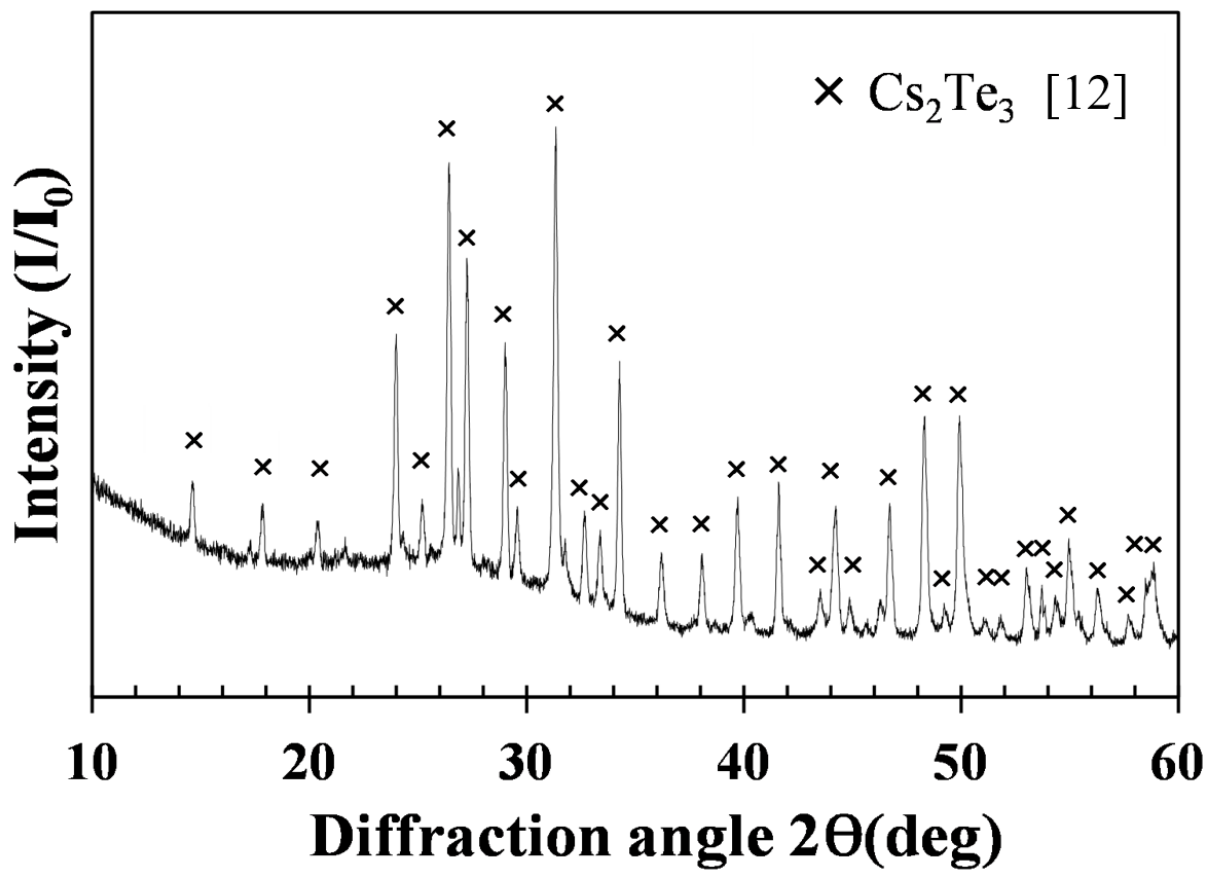


Figure 5. An X-Ray Diffraction pattern of the Cs-Te corrosive compound.

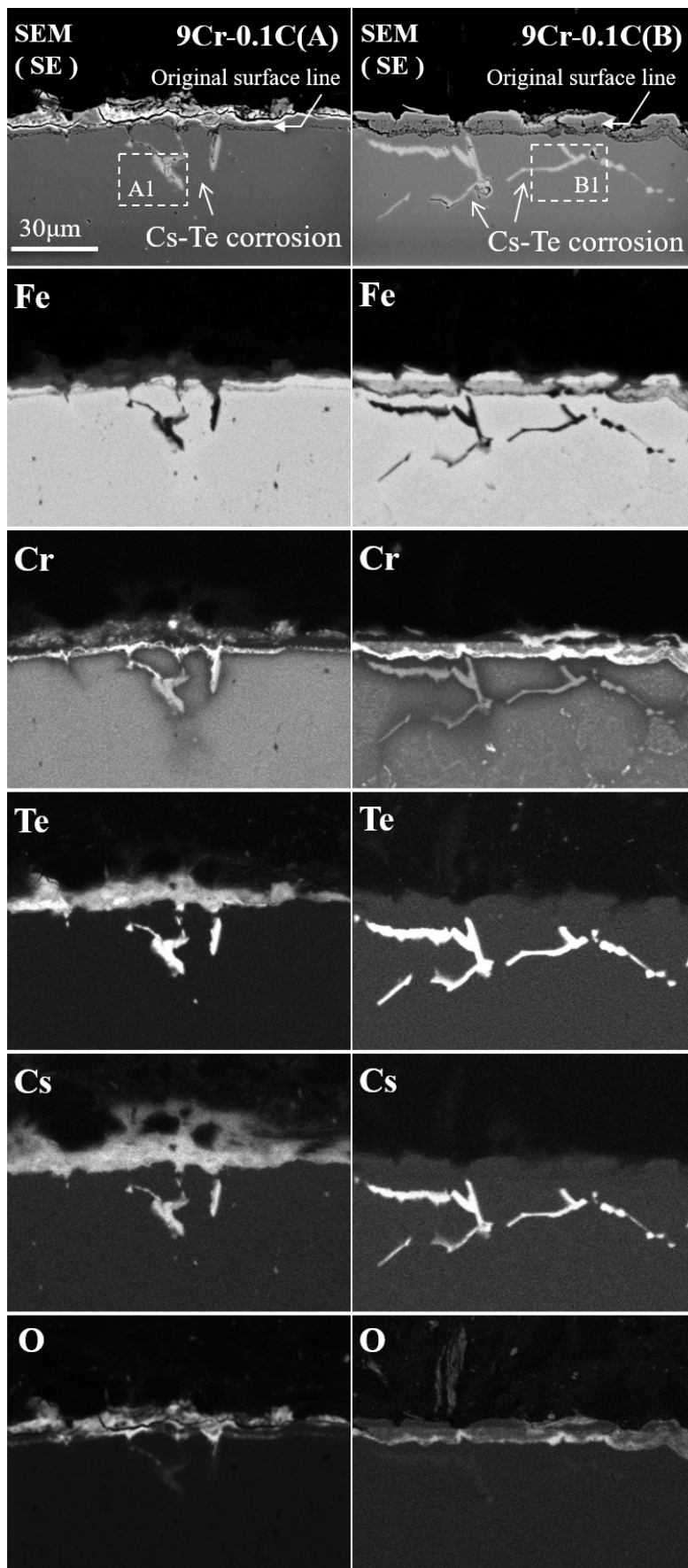


Figure 6 (a). SEM images and EDS mapping images of cross-section of the specimens after the corrosion test.

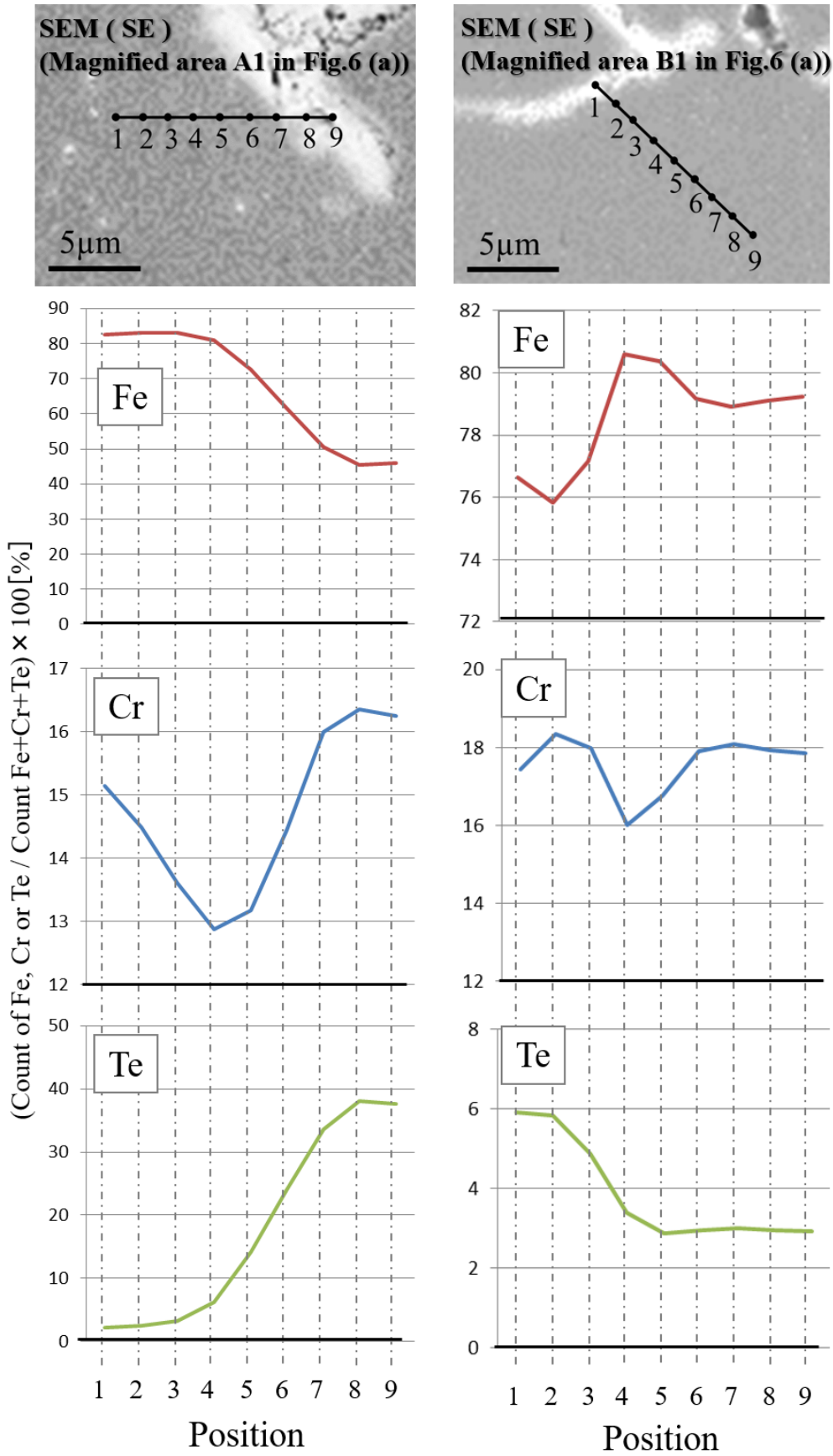
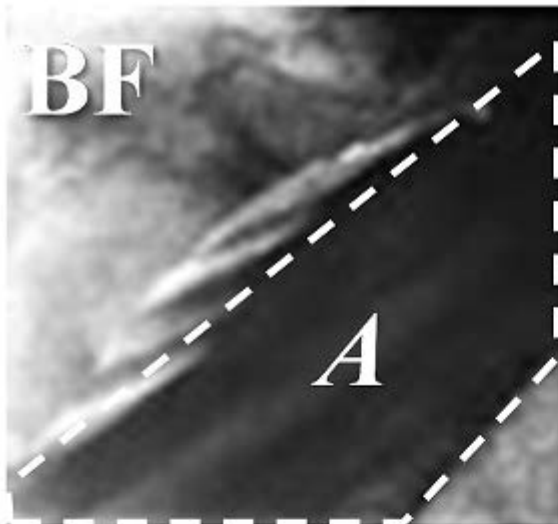


Figure 6 (b). Magnified SEM images and EDS line profiles of area A1 and B1 in Figure 6 (a).



— 0.5 $\mu\text{m}$

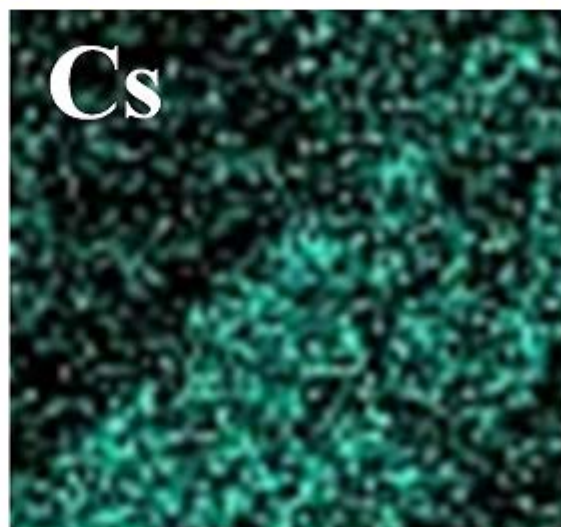
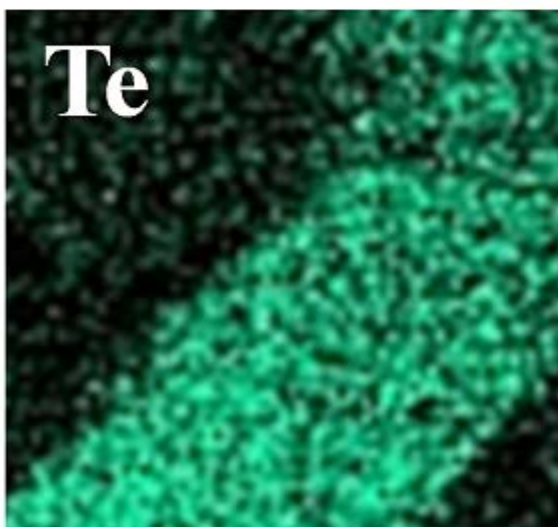
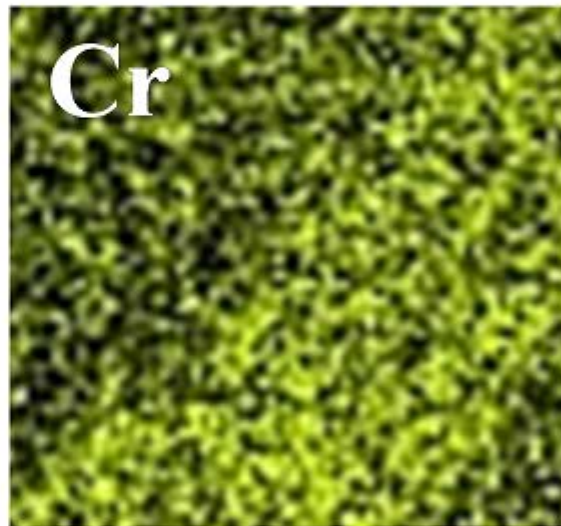


Figure 7 (a). A TEM image and EDS mapping images of a part of corroded area in 9Cr-0.1C(A).

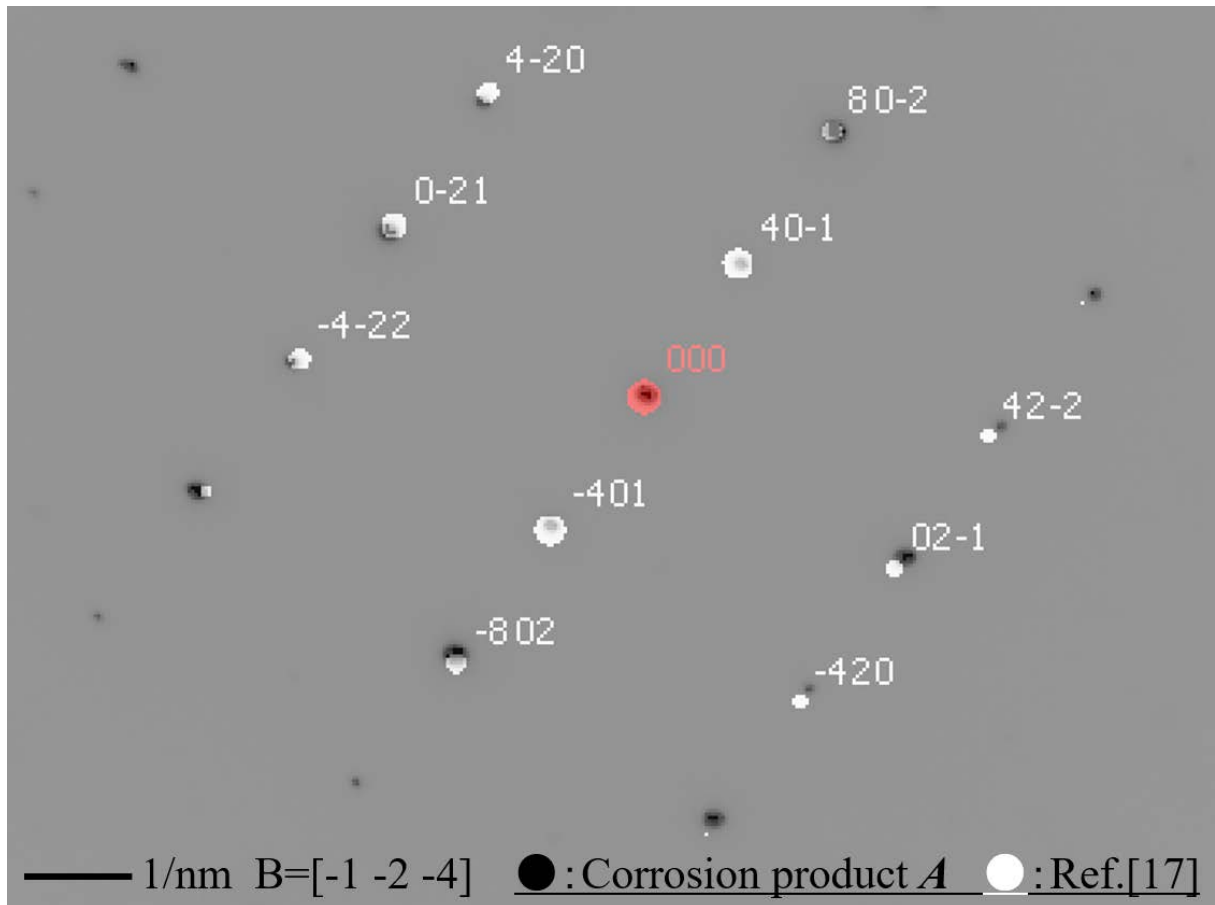


Figure 7 (b). An electron diffraction pattern of the corrosion product *A* in Figure 7 (a).

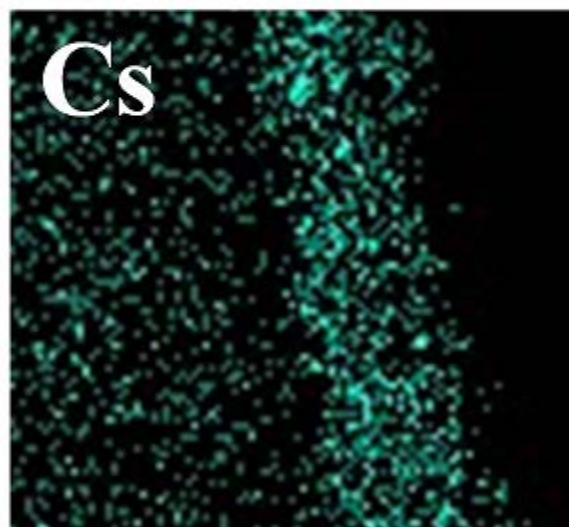
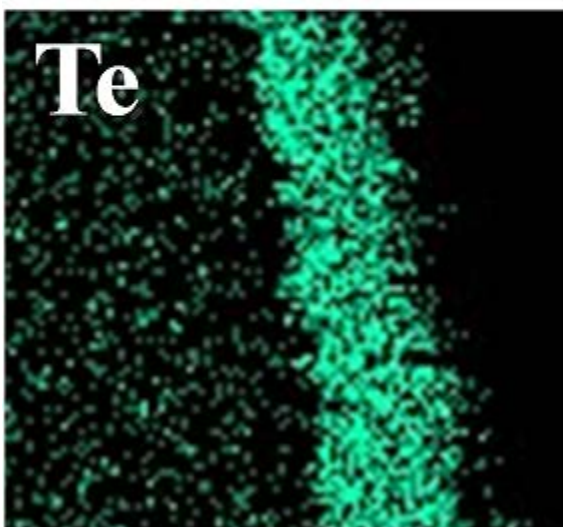
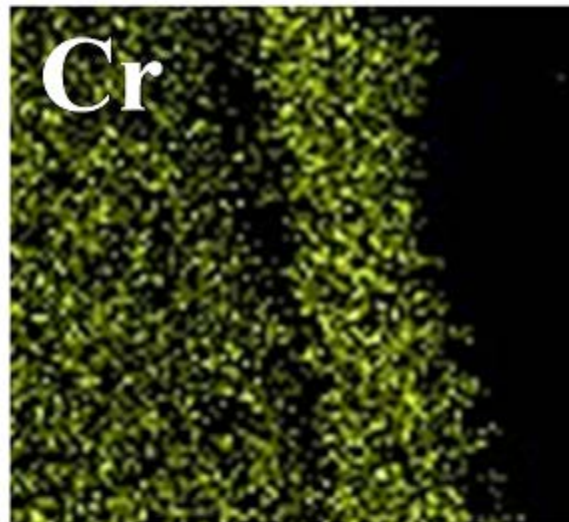
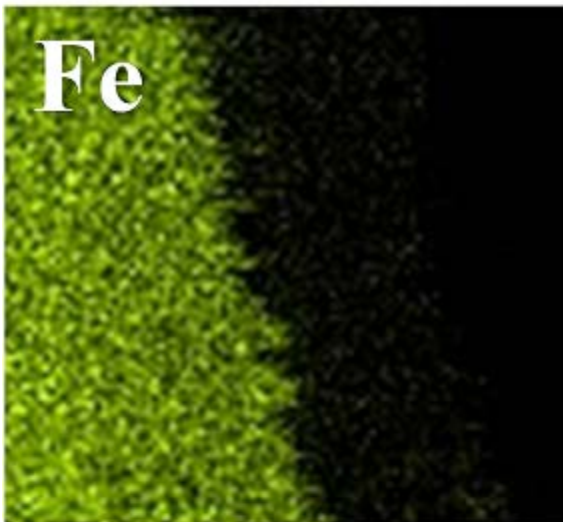
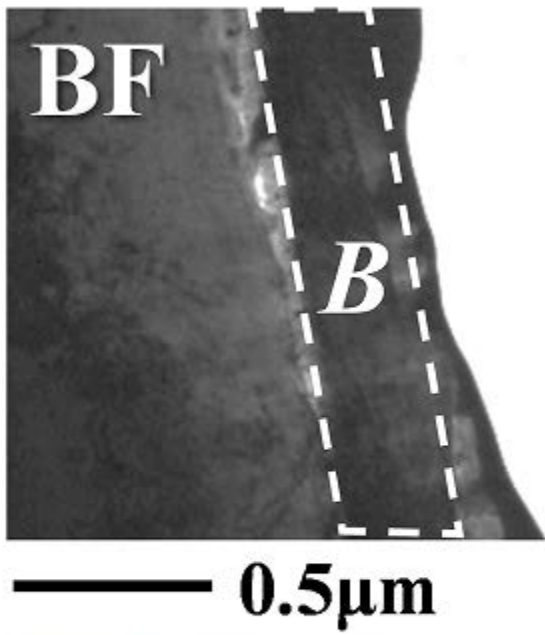


Figure 8 (a). A TEM image and EDS mapping images of a part of corroded area in 9Cr-0.1C(B).

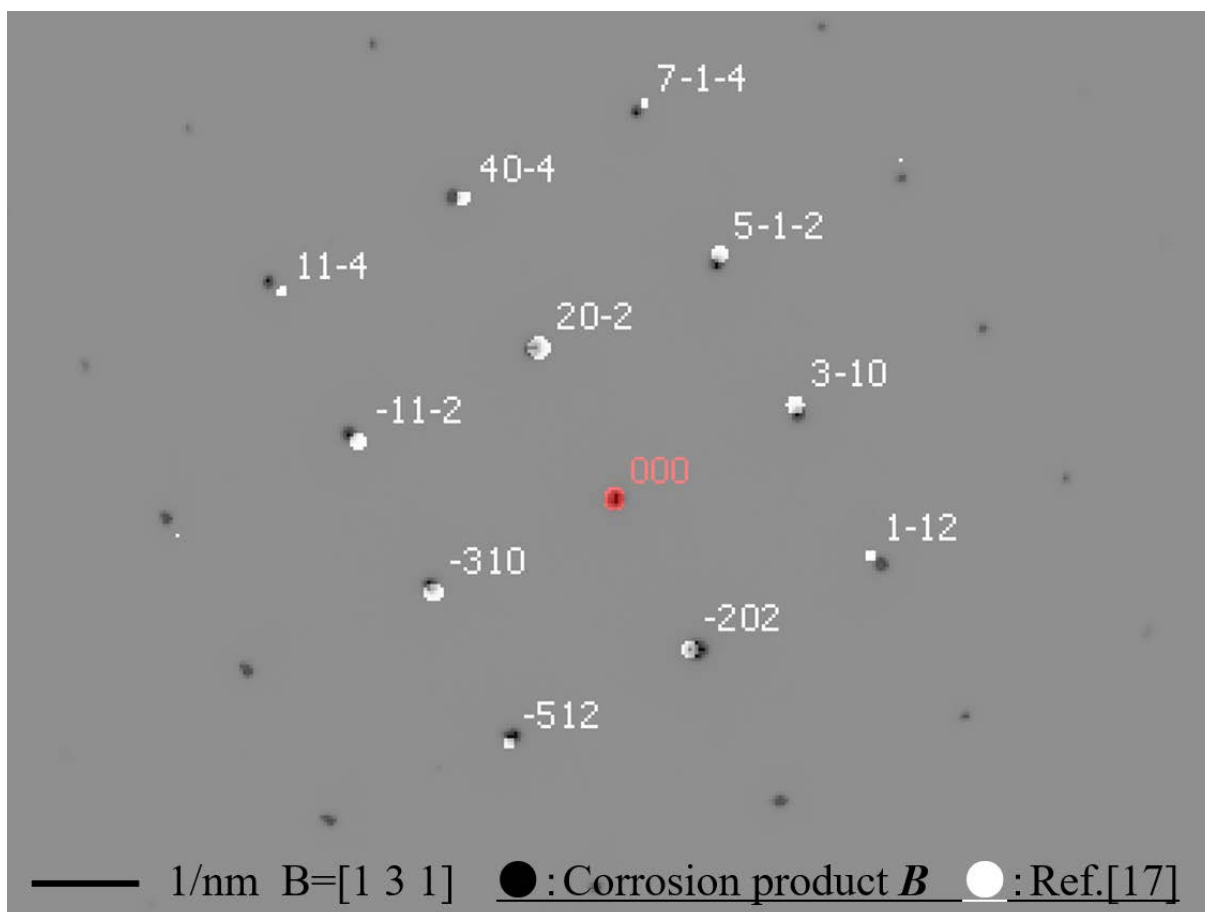


Figure 8 (b). An electron diffraction pattern of the corrosion product *B* in Figure 8 (a).

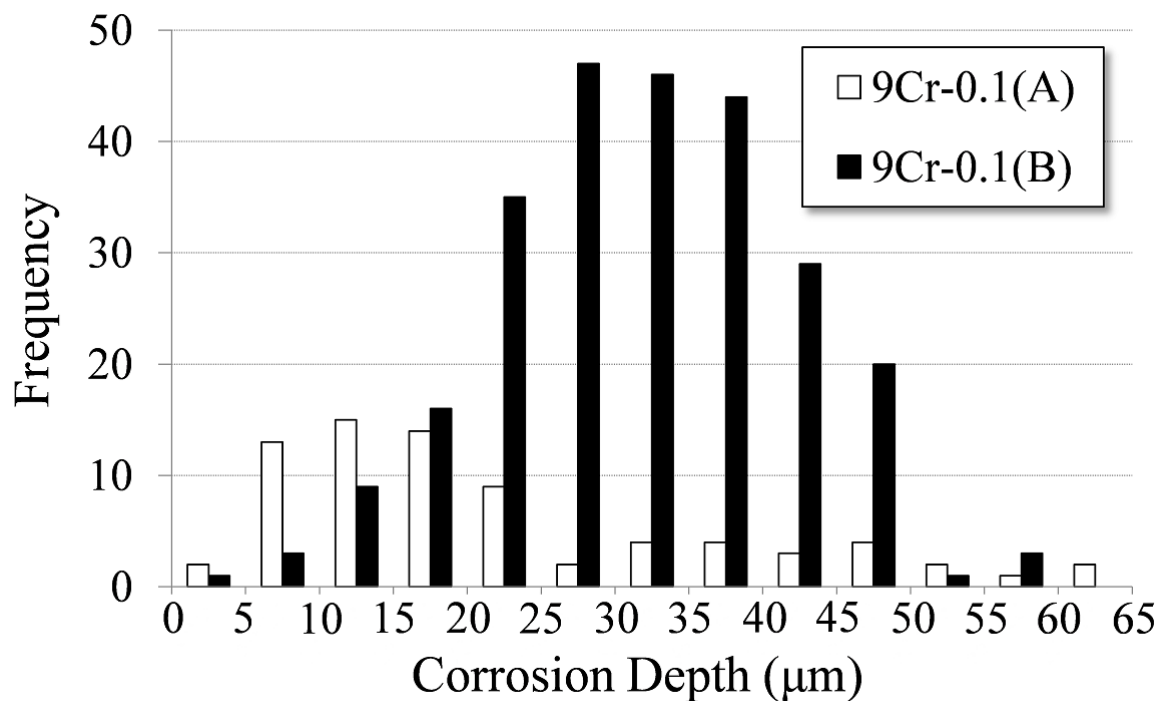


Figure 9. Histograms of corrosion depth in 9Cr-0.1C(A) and (B).

**Figure captions (two column)**

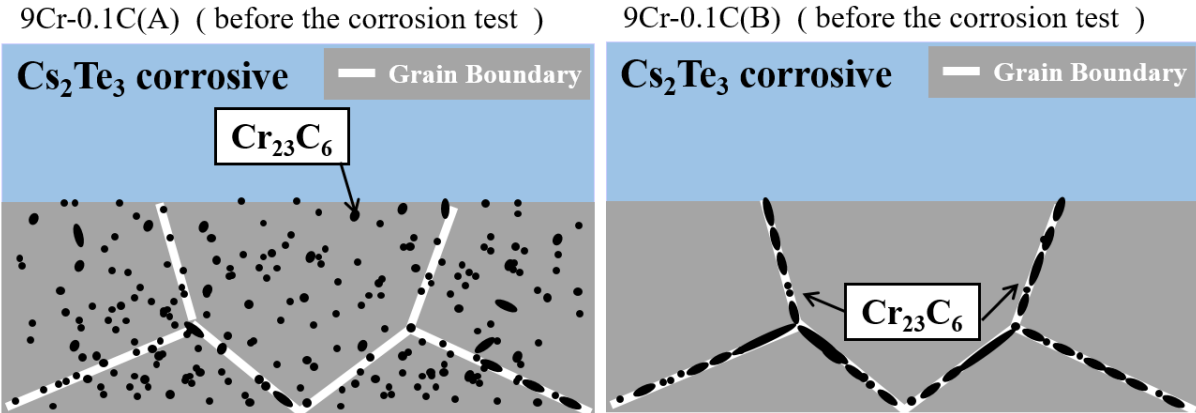


Figure 10 (a). Illustrations of cross-section of the specimens before the corrosion test.

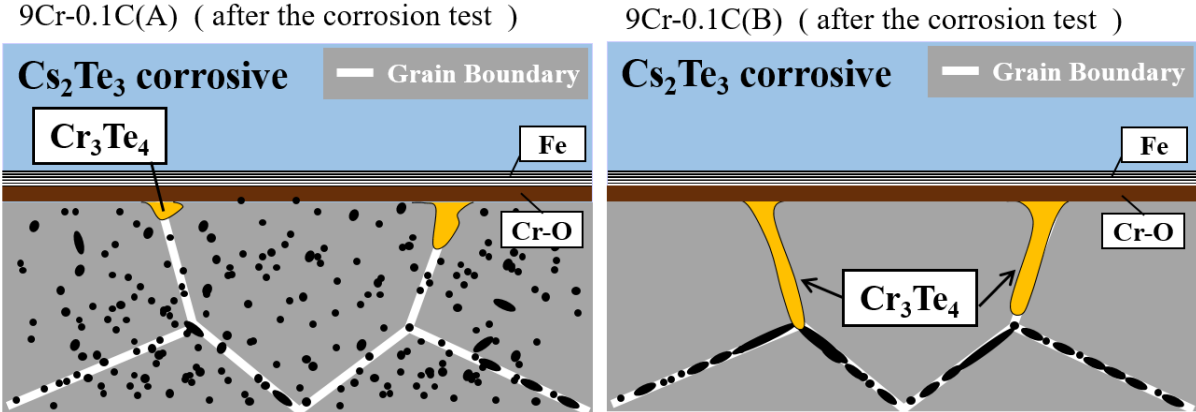


Figure 10 (b). Illustrations of cross-section of the specimens after the corrosion test.